WOOD RESEARCH
65 (5): 2020
737-746
doi.org/10.37763/wr.1336-4561/65.5.737746

IN SITU HYDROTHERMAL SYNTHESIS OF MnO_2 NANOWIRES/WOOD DERIVED ACTIVATED CARBON HOLLOW FIBERS COMPOSITE AND ITS APPLICATION IN SUPERCAPACITOR

Liyan Ma
Chinese Academy of Tropical Agricultural Sciences
China

Lina Wang, Xiaojun Ma
Tianjin University of Science and Technology
China

Jianing Li
Chinese Academy of Tropical Agricultural Sciences
China

(Received October 2019)

ABSTRACT

Composite electrode material composed of MnO_2 nanowires and wood-derived activated carbon hollow fibres (Mn@ACHFs) was successfully fabricated by in situ hydrothermal method. In this work, MnO_2 nanowires were developed by adjusting the mass ratio of potassium permanganate and wood activated carbon hollow fibres (ACHF). The ACHF with hierarchical porous structure served not only as the support for the growth of MnO_2 particles, but also as the electric double layer capacitance for the composite electrode. The Mn@ACHFs exhibited an outstanding specific capacitance of 420 $F \cdot g^{-1}$ at 1 $A \cdot g^{-1}$ and cycle stability with 99.7% capacitance retention after 5000 cycles at 5 $A \cdot g^{-1}$. Electrochemical characteristics of the prepared composites are attributed to the synergetic effect of the double layer capacitance of the hierarchical porous ACHF and the layered structure of MnO_2, which can efficiently enhance the conductivity and stability of the electrodes.

KEYWORDS: Wood waste, MnO_2 nanowires, activated carbon hollow fibres, supercapacitors.

INTRODUCTION

The conversion of agricultural and forestry resources into carbon-based new energy materials is an important strategy that can add value to cellulose, hemicellulose and lignin in biomass components and enable their efficient utilization (Pandolfo et al. 2006, Duan et al. 2017). Recently, biomass-derived carbons have much more strengths such as abundant, sustainable and low-cost source, which are usually the wastes from natural source, such as wood processing wastes (Liu et al. 2013, Doczekalska et al. 2017, Ho et al. 2018, Li et al. 2013, 2018, 2019). Additionally, more and more wood-based carbon materials became the potential applications using as supercapacitor processing components in portable devices and electric vehicles, due to high surface area, good electrical conductivity and excellent physicochemical stability (Li et al. 1998, Bhattacharjya et al. 2014, Chen et al. 2017).

However, previous studies showed that wood carbon materials exhibited moderate capacitive performance (Ma et al. 2018, Ma et al. 2019). Therefore, a large amount of research has been devoted to maximally improving the low specific capacitance of biomassed carbon materials by adding heteroatoms (Peng et al. 2016) or transition metal oxides (TMO) (Nagaraju et al. 2017, Jiang et al. 2018). TMO has the favorable capacitive characteristics and environmental friendliness (Augustyn et al. 2014). Moreover, it can also introduce considerable the pseudocapacitance for the composite electrode, which effectively improving the specific capacity and conductivity of the electrode. Among TMO, manganese dioxide (MnO_2) is a promising tantalum capacitor material for supercapacitors and is expected to improve the capacitive performance of wood-based carbon materials due to the high theoretical capacity, low cost, non-toxicity and environmental protection (Chinnappan et al. 2017).

In this work, composite electrode material composed of MnO_2 nanowires and wood-derived activated carbon hollow fibres (Mn@ACHFs) was successfully synthesized by liquefaction, melt spinning, steam activation methods and in situ composite hydrothermal method. The morphology, microstructure, pore texture and surface area of the Mn@ACHFs were investigated in detail. Moreover, the electrochemical performances of the composites were determined by constant current charge-discharge, cyclic vohammetry and AC impedance, respectively. This work demonstrates an avenue for the design of economic and sustainable energy storage materials from forestry and agricultural wastes.

MATERIAL AND METHODS

Wood waste (sawdust) was obtained from Tianjin Nanyang furniture Co. Ltd (China). Prior to use, sawdust were air dried, ground in high-speed rotary cutting mill, and then screened to give the particle size of $0.2 < Dp < 0.8$ mm. Phenol, hexamethylenetetramine, formaldehyde (CH_2O, 37 wt%), hydrochloric acid (HCl, 37 wt%), phosphoric acid (H_3PO_4, 37 wt%), methanol (CH_3OH, 99 wt%) were purchased Tianjin Jinghong Chemical Reagent (China).

Wood-derived activated carbon hollow fibres (ACHF) were prepared according the previous reports (Ma et al. 2019, Ma et al. 2018). A mixture composed of dried wood powder and phenol at a mass ratio of 1 : 6 was liquefied for 2.5 h at 160°C with 8% phosphoric acid (based on the mass ratio of phenol). The as-prepared liquefied wood was placed into a reaction tube with 5% hexamethylenetetramine (based on the mass ratio of liquefied wood) as the synthetic material. The mixture was heated from room temperature to 130°C in 40 min to prepare the spinning solution. The spinning solution was placed into a spinning machine, and the initial fibers were

prepared by melt-spinning. The spun filaments were half-cured by soaking in an acid solution CH_2O and HCl (1:1 by volume) as main components at 95°C for 5 h, washed with distilled water and finally dried at 90°C for 45 min to obtain the half-cured fibers. Subsequently, the half-cured fibers were immersed into 18.5% methanol solution at 50°C for 0.5 h, washed with distilled water and dried to obtain the hollow half-cured fibers. Then, the hollow fiber samples (HFs) were obtained after the second curing, washed with distilled water and dried at 90°C for 40 min. The as-prepared HFs was activated in a tubular furnace with a temperature program from room temperature to 800°C using a heating rate of 5 °C·min^{-1} under N_2 (200 cm^3·min^{-1}), held isothermally for 40 min under a steam flow of 8 g·min^{-1}, and then cooled to room temperature to obtain the ACHF.

Mn@ACHFs were prepared by a facile one-step hydrothermal reaction method. 0.8 g of $KMnO_4$ was dissolved in 100 mL of deionized water, and then added some ACHFs at 80°C for 6h. After washing several times with deionized water and absolute ethanol, the samples were dried at 80°C for 12h to obtain the Mn@ACHFs. According to the mass ratio of $KMnO_4$ and ACHFs (10:100, 40:100, 70:100, 100:100, 130:100), the prepared composites were named as 10Mn@ACHF, 40Mn@ACHF, 70Mn@ACHF, 100Mn@ACHF and 130Mn@ACHF, respectively.

The morphology and energy dispersive spectroscopy (EDS) mapping were obtained by scanning electron microscopy (SEM, NanoSEM430). The N_2 adsorption–desorption isotherms, the surface area and the porosity of the samples were obtained at 77 K using an ASAP 2020 automatic apparatus (Micromeritics Instrument Co., Norcross, GA, USA).

Electrochemical measurements were carried out on an electrochemical workstation (Autolab PGSTAT 302N, Metrohm, Netherlands) using 6 mol·L^{-1} KOH as electrolyte under a three-electrode system at room temperature. To fabricate the working electrode, Mn@ACHFs composite, carbon black, and polytetrafluoroethylene (PTFE) binder were mixed with the weighting ratio of 70:15:15, then compressed onto a nickel foam followed by drying at 80°C for 12 h. Finally, the as-prepared electrode plate was further compressed under 10 MPa to get the Mn@ACHFs composite-working electrode.

The working electrodes have been prepared by mixing 70 wt% active electrode material (Mn@ACHFs), 15 wt% carbon black and 15 wt% PTFE binder together until to become the viscous slurry, then compressed onto a nickel foam followed by drying at 80°C for 12 h. Finally, the as-prepared electrode plate was further compressed under 10 MPa to get the Mn@ACHFs composite-working electrode. The cyclic voltammetry (CV) tests were measured from -1 to 0 V with scan varied rates of 5 - 100 m·V·s^{-1}. Electrochemical impedance spectroscopy (EIS) tests were measured from 10 mHz to 100 kHz at the open circuit potential. The galvanostatic charge–discharge measurement of MnO_2@ACHFs electrodes was measured in the potential range from 0 to 1 V at current densities of 1, 2, 3, 5, 10 and 15 A·g^{-1}. The specific capacitance (C_g) was calculated from the galvanstatic charge-discharge (GCD) values according to the Eq. (1):

$$C_g = I \cdot \Delta t / m \cdot \Delta V \quad (F \cdot g^{-1}) \tag{1}$$

where: I (A), ΔV (V) and Δt (s) is discharge current, voltage and time, resp.
m (g) corresponds to the weight of active material on the nickel foam.

The symmetric supercapacitors were assembled with two equal-power electrodes using non-woven polypropylene mat as separator, and evaluated in 6M KOH. The C_g was calculated according to the Eq. (2):

$$C_g = 4 \cdot I \cdot \Delta t / m \cdot \Delta V \quad (F \cdot g^{-1}) \tag{2}$$

where: I (A), ΔV (V), m (g) and Δt (s) are described as in Eq. (1).

RESULTS AND DISCUSSION

Fig. 1 shows the morphology and of all samples. The surface morphology of Mn@ACHFs gradually changed with the increase of manganese loading. Initially, a small amount of MnO_2 nanowires and the grain particles with a diameter of approximately 50 nm were generated (Fig. 1a). Then, these grains were completely transformed into MnO_2 nanowires with the diameter of dozens of nanometres and length of hundreds of nanometres after the increase in the reactant proportion (Fig. 1b). The nanowires generated on the surface of 70Mn@ACHF are radially cross-linked and wound to form an accessible porous structure with wider ionic diffusion tunnels that is highly favourable for the rapid insertion/extraction of electrolyte ions (Jian et al. 2017, Ma et al. 2019). However, flower-sphere-like MnO_2 nanowires were generated on the surface of the ACHF after a further increase in the proportion of the reactants (Fig. 1c-d). Excessive accumulation is not conducive to the transport of electrolyte ions, and also covers the surface pores of ACHF. EDX spectrum analysis also indicated that some heteroatoms N, P and O were well-distributed in various samples (Fig. 1e-i), which is derived from chemical substances such as hexamethylenetetramine and phosphoric acid during wood liquefaction.

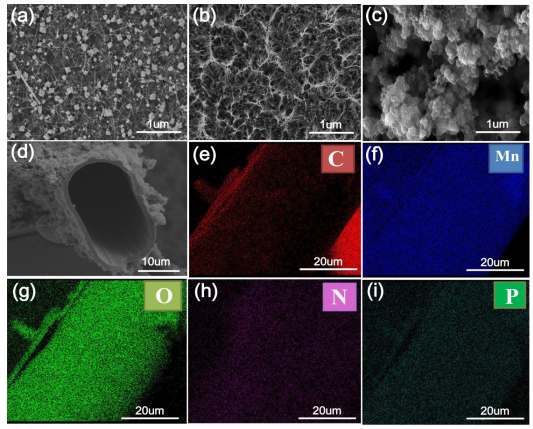

Fig.1: SEM images of Mn@ACHFs: a) 10Mn@ACHF, b)70Mn@ACHF, c) 100Mn@ACHF, d) section SEM images of 100Mn@ACHF, e-i) the EDX spectra of 70Mn@ACHF.

Fig. 2 shows the N_2 adsorption/desorption isotherms of all samples. The isotherm of ACHF is type I according to the IUPAC classification. As can be seen from Fig. 2, the adsorption capacity of Mn@ACHFs is lower than the ACHF, because of MnO_2 covering the surface of ACHFs, blocking the majority of the pores. With MnO_2 content increasing, the isotherms of Mn@ACHFs have a glacis knee and the slope of the plateau increases due to multilayer adsorption (Fig. 2a). The widely opened knees and the slight hysteresis loops indicate the presence of a considerable amount of small mesopores in Mn@ACHFs, which is due to the reaction between $KMnO_4$ and C increases the number of micropores and when the amount of the reactants increases, the micropores are further eroded by the reactants to form more mesopores.

The increase in the number of the mesopores is favourable for the dispersion of the electrolyte ions. The pore size distribution exhibits sharp peaks at ~2.5 nm (Fig. 2b), which illustrates the narrow pore size distribution in composite electrode materials, resulting in better electrochemical performance (Wang et al. 2018).

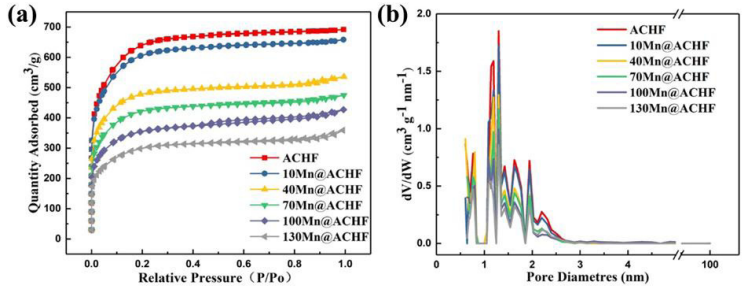

Fig. 2: Nitrogen adsorption-desorption isotherms (a) and pore size distribution curves, (b) for Mn@ACHFs.

The electrochemical properties of the Mn@ACHFs were tested in a 6 M KOH solution in a three-electrode system. The comparative cyclic voltammetry (CV) curves of Mn@ACHFs at a constant scan rate of 10 $m{\cdot}V{\cdot}s^{-1}$ and the GCD curves of the samples at 1 $A{\cdot}g^{-1}$ show that the CV curve area and specific capacitance of 70Mn@ACHF are clearly greater than those of the other samples, indicating the enhancement in the capacitance and acceleration of ion transport (Fig. 3a,b). The electrochemical performance decreased with the overloading of MnO_2 due to the flower-sphere-like MnO_2 nanowires generated on the surface of the ACHF blocking electrolyte ion insertion/extraction, and due to the overloaded of MnO_2 completely covering the pores on the ACHF surface. Moreover, a large number of cavities were formed by the radial growth and cross-linking of the MnO_2 nanowires on the ACHF, enhancing the ion diffusion into the MnO_2 layer. Thus, the synergistic effects of the high specific pseudo-capacitance of the MnO_2 nanowires layer and highly conductive ACHF give rise to high capacitor performance. As shown in Fig. 3c, the CV curves of the 70Mn@ACHF is quasi-rectangular shape with one redox peaks with the increasing of the scan rate from 10 to 500 $mV{\cdot}s^{-1}$, indicating that the capacitance consisted of electrochemical double-layer capacitance and pseudocapacitance. GCD curves of 70Mn@ACHF at different current densities are shaped like arc lines, which are due to the reversible pseudfaradaic reactions (Fig. 3d). Among all of the electrodes, 70Mn@ACHF has the highest specific capacitance that reaches 420 $F{\cdot}g^{-1}$ at 1 $A{\cdot}g^{-1}$ (Fig. 3e), which is competitive with those of the recently reported supercapacitors fabricated on carbon fibres (Ko et al. 2018, Ye et al. 2017, Sun et al. 2017). Moreover, the specific capacitance of 70Mn@ACHF was higher than that of the other samples for all of the various current densities. Considering its superior well-developed porous structure and good conductivity, it is concluded 70Mn@ACHF has the most remarkable electrochemical properties compared to the other prepared carbon materials. Notably, slight humps were observed at approximately -0.3 V in the CV curves of ACHF due to the redox reactions of the N, P and O heteroatoms.

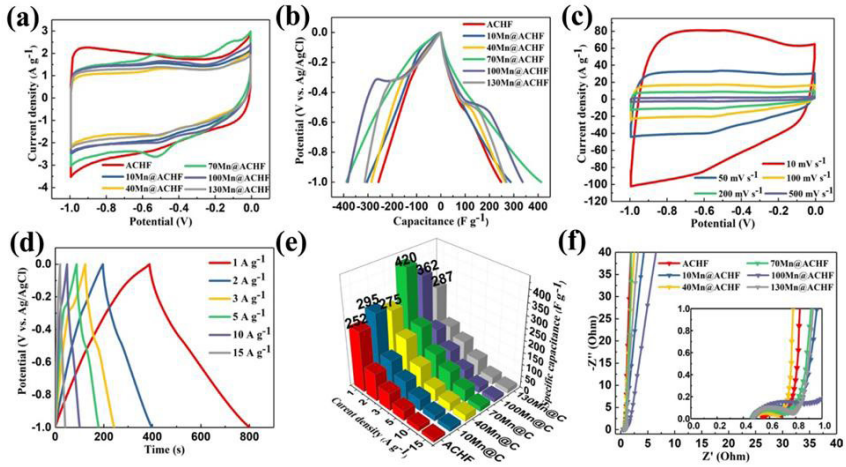

Fig. 3: Electrochemical measurements of Mn@ACHFs performed in a three-electrode system in 6 M KOH: (a) CV curves at 10 mV s^{-1}; (b) GCD curves at 1 A g^{-1}; (c) CV curves of 70Mn@ACHF at different scan rates; (d) GCD curves of 70Mn@ACHF at different current densities; (e) Specific capacitance at different current densities; (f) Nyquist plots (inset: magnified figure of the arc part).

EIS data were measured to examine the frequency response characteristics of the electrodes, and the obtained Nyquist plots are shown in Fig. 3f. The vertical lines revealed the outstanding double-layer capacitance properties of Mn@ACHFs due to the rapid ion diffusion in the materials' internal structure (Demir et al. 2018). Clearly, the slope of 70Mn@ACHF is higher than that of the ACHF, which means that the 70Mn@ACHF has lower diffusive resistance and faster ion transport than ACHF; this is due to the cross-linked and intertwined homogeneous porous structure of manganese dioxide on the ACHF surface. The ohmic resistance (Rs) values of 0.55, 0.41, 0.47, 0.39, 0.40 and 0.58 Ω are obtained for ACHF, 10Mn@ACHF, 40Mn@ACHF, 70Mn@ACHF, 100Mn@ACHF and 130Mn@ACHF, respectively. Obviously, the small RS values for 70Mn@ACHF is most likely due to its excellent conductivity (Ho et al. 2018). With the exception of 130Mn@ACHF, the Rs values of the other samples are lower than that of ACHF implying good synergy between MnO_2 and ACHF. A semicircular part of the Mn@ACHFs spectra display increasingly higher charge transfer resistance values as the manganese dioxide loading increased, which is attributed to the low conductivity of manganese dioxide.

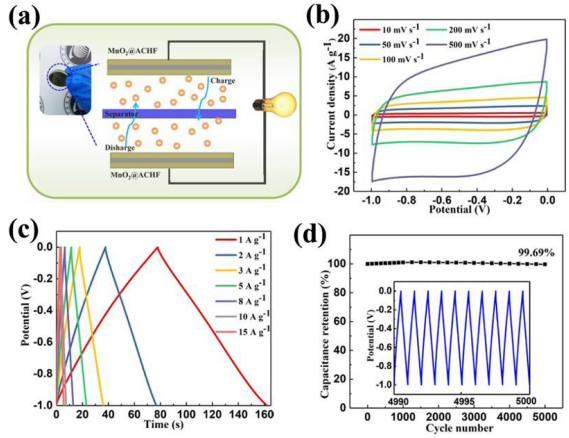

Fig. 4: Electrochemical measurements of 70Mn@ACHF in a two-electrode system in 6 M KOH: (a) CV curves at different scan rates; (b) GCD curves at different current densities; (c) cycling stability in a symmetric supercapacitor at 5 A·g^{-1} over 5000 cycles; (d) schematic diagram of button battery structure.

A two-electrode symmetric supercapacitor was measured in 6 M KOH in order to further study the cycle life of Mn@ACHFs samples used for electrochemical energy storage (Fig. 4a). The almost symmetric and rectangular shaped CV curves and the symmetrical triangular-like GCD curves reveal its ideal electrochemical performance (Fig. 4b-c). The 70Mn@ACHF displays a specific capacitance (338 F·g^{-1}) at 1 A·g^{-1}, and even after more than 5000 cycles (Fig. 4d), the capacitance retention is still as high as 99.7%, revealing the excellent long-term electrochemical cycling stability.

CONCLUSIONS

A series of Mn@ACHFs samples were prepared from wood waste by liquefaction, melt spinning, steam activation methods and an in situ hydrothermal method. The electrochemical of the composites are related to the phase content of MnO_2, surface area, pore size and their distributions. The 70Mn@ACHF sample exhibited a high capacitance (420 F·g^{-1} at 1 A·g^{-1} current densities) in the 6 M KOH solution. Overall, it is concluded that sustainable biomass-derived carbon fibres from forestry and agricultural residues are promising candidates for use as electrochemical energy storage materials. The synergetic effect of the layer structured MnO_2 and the hierarchical porous ACHF from wood waste efficiently enhance the conductivity and stability of the electrodes.

ACKNOWLEDGMENT

This research has been financially supported by Opening Project Fund of Key Laboratory of Biology and Genetic Resources of Rubber Tree, Ministry of Agriculture and Rural Affairs, P. R. China/ State Key Laboratory Breeding Base of Cultivation & Physiology for Tropical Crops/ Danzhou Investigation & Experiment Station of Tropical Crops, Ministry of Agriculture and Rural Affairs, P. R. China (RRI-KLOF202001), and the National Natural Science Foundation

of China (No. 31270607).

REFERENCES

1. Augustyn, V., Simon, P., Dunn, B., 2014: Pseudocapacitive oxide materials for high-rate electrochemical energy storage. Energy & Environmental Science 7(5): 1597-1614.
2. Bhattacharjya, D., Yu, J.S., 2014: Activated carbon made from cow dung as electrode material for electrochemical double layer capacitor. Journal of Power Sources 262: 224-231.
3. Chen, C., Zhang, Y., Li, Y., Dai, J., Song, J., Yao, Y., Gong, Y., Kierzewski, I., Xie, J., Hu, L., 2017: All-wood, low tortuosity, aqueous, biodegradable supercapacitors with ultra-high capacitance. Energy & Environmental Science 10(2): 538-545.
4. Chinnappan, A., Bandal, H., Kim, H., Ramakrishna, S., 2017: Mn nanoparticles decorated on the ionic liquid functionalized multiwalled carbon nanotubes as a supercapacitor electrode material. Chemical Engineering Journal 316: 928-935.
5. Demir, M., Tessema, T.D., Farghaly, A.A., Nyankson, E., Saraswat, S.K., Aksoy, B., Islamoglu, T., Collinson, M.M., El-Kaderi, H.M., Gupta, R.B., 2018: Lignin-derived heteroatom-doped porous carbons for supercapacitor and CO_2 capture applications. International Journal of Energy Research 42(8): 2686-2700.
6. Doczekalska, B., Pawlicka, A., Kusmierek, K., Swiatkowski, A., Bartkowiak, M., 2017: Adsorption of 4-chlorophenol from aqueous solution on activated carbons derived from hornbeam wood. Wood Research: 62(2): 261-272.
7. Duan, X.H., Srinivasakannan, C., Wang, X., Wang, F., Liu, X.Y., 2017: Synthesis of activated carbon fibers from cotton by microwave induced H_3PO_4 activation. Journal of the Taiwan Institute of Chemical Engineers 70: 374-381.
8. Ho, H.C., Goswami, M., Chen, J., Keum, J.K., Naskar, A.K., 2018: Amending the structure of renewable carbon from biorefinery waste-streams for energy storage applications. Scientific reports 8(1): 8355.
9. Jian, X., Liu, S., Gao, Y., Zhang, W., He, W., Mahmood, A., Subramaniyam, C.M., Wang, X., Mahmood, N., Dou, S.X., 2017: Facile synthesis of three-dimensional sandwiched MnO_2@ GCs@ MnO_2 hybrid nanostructured electrode for electrochemical capacitors. ACS Applied Materials & Interfaces 9(22): 18872-18882.
10. Jiang, J., Zhu, K., Fang, Y., Wang, H., Ye, K., Yan, J., Wang, G., Cheng, K., Zhou, L., Cao, D., 2018: Coralloidal carbon-encapsulated CoP nanoparticles generated on biomass carbon as a high-rate and stable electrode material for lithium-ion batteries. Journal of Colloid and Interface Science 530: 579-585.
11. Ko, W.Y., Liu, Y.C., Lai, J.Y., Chung, C.C., Lin, K.J., 2018: Vertically standing MnO_2 nanowalls grown on AgCNT-modified carbon fibers for high-performance supercapacitors. ACS Sustainable Chemistry & Engineering 7(1): 669-678.
12. Li, D.N., Li, J.N., Ma, X.J., 2019: Sustainable activated carbon hollow fibers from liquefied rubber wood (*Hevea brasiliensis*) and its adsorption of organic matter from solution. WoodResearch: 64(2): 317-324.
13. Li, D.N., Li, J.N., Ren, B.Y., Li, T.T., Ma, X.J., 2018: Synthesis and characterization of wooden magnetic activated carbon fibers with hierarchical pore structures. Polymers 10: 435.
14. Li, D.N., Ma, X.J., 2013: Preparation and characterization of activated carbon fibers from liquefied wood. Cellulose 20(4): 1649-1656.
15. Li, C.Y., Wang, W.J., Wang, Y.L., Jiang, X.Q., Han, L.M., 1998: Antibacterial pitch-based

activated carbon fiber supporting silver. Carbon 36(1-2): 61-65.
16. Liu, W.J., Zhao, G.J., 2013: preparation of wooden activated carbon fibers using different steam flow. Wood Research: 58(4): 533-542.
17. Ma, L.Y., Li, J.N., Ma, X.J., 2019: Improvement of electrochemical properties of activated carbon hollow fibers from liquefied wood by charcoal power. Materials Letters 255: 126544.
18. Ma, L.Y., Li, J.N., Ma, X.J., 2019: Preparation and CO_2 and H_2 adsorption of activated carbon hollow fibers from rubber wood (*Hevea brasiliensis*). BioResources 14(4): 9755-9765.
19. Ma, X., Ding, C., Li, D., Wu, M., Yu, Y., 2018: A facile approach to prepare biomass-derived activated carbon hollow fibers from wood waste as high-performance supercapacitor electrodes. Cellulose 25(8): 4743-4755.
20. Nagaraju, G., Cha, S.M., Yu, J.S., 2017: Ultrathin nickel hydroxide nanosheet arrays grafted biomass-derived honeycomb-like porous carbon with improved electrochemical performance as a supercapacitive material. Scientific reports 7: 45201.
21. Pandolfo, A., Hollenkamp, A., 2006: Carbon properties and their role in supercapacitors. Journal of Power Sources 157(1): 11-27.
22. Peng, H., Ma, G., Sun, K., Zhang, Z., Yang, Q., Lei, Z., 2016: Nitrogen-doped interconnected carbon nanosheets from pomelo mesocarps for high performance supercapacitors. Electrochimica Acta 190: 862-871.
23. Sun, B.Q., Chen, Y., Ma, X.J., 2017: The influence of calcination temperature on the structure and visible light photocatalysis performance of Mn-TiO_2-loaded wooden activated carbon fibers. Wood and Fiber Science 49(4): 436-443.
24. Wang, J., Dong, L., Xu, C., Ren, D., Ma, X., Kang, F., 2018: Polymorphous supercapacitors constructed from flexible three-dimensional carbon network/polyaniline/MnO_2 composite textiles. ACS Applied Materials & Interfaces 10(13): 10851-10859.
25. Ye, Z., Li, T., Ma, G., Peng, X., Zhao, J., 2017: Morphology controlled MnO_2 electrodeposited on carbon fiber paper for high-performance supercapacitors. Journal of Power Sources 351: 51-57.

Liyan Ma, Jianing Li*
Chinese Academy of Tropical Agricultural Sciences
Rubber Research Institute
Ministry of Agriculture Key Laboratory of Biology and Genetic Resource
Utilization of Rubber Tree
State Key Laboratory Breeding Base of Cultivation
and Physiology for Tropical Crops
Danzhou 571700
China
*Corresponding author: ljn206@163.com

Lina Wang, Xiaojun Ma
Tianjin University of Science and Technology
College of Light Industry Science and Engineering
Tianjin 300222
China